The Astronomical Journal, 162:29 (11pp), 2021 July https://doi.org/10.3847/1538-3881/abf8b0
© 2021. The American Astronomical Society. All rights reserved.

Evaluating the Thickness and Stratigraphy of Ejecta Materials at the Chang'e-4 Landing Site

Luyuan Xu[1,2], Xunyu Zhang[1,2], Le Qiao[3], and Jialong Lai[1,2,4]
[1] State Key Laboratory of Lunar and Planetary Sciences, Macau University of Science and Technology, Macau, People's Republic of China; xyzhang@must.edu.mo
[2] CNSA Macau Center for Space Exploration and Science, Macau, People's Republic of China
[3] Shandong Key Laboratory of Optical Astronomy and Solar-Terrestrial Environment, School of Space Science and Physics, Institute of Space Sciences, Shandong University, Weihai, Shandong 264209, People's Republic of China; leqiao.geo@gmail.com
[4] School of Science, Jiangxi University of Science and Technology, Ganzhou, People's Republic of China
Received 2020 December 8; revised 2021 April 14; accepted 2021 April 14; published 2021 June 24

Abstract

The landing site of China's Chang'e-4 (CE-4) probe is located on the mare basalts on the floor of the Von Kármán crater on the lunar far side. The Von Kármán crater is inside the ancient and highly cratered South Pole–Aitken basin, which has experienced complex emplacement sequences of both near and distant ejecta materials. These issues complicated the interpretation of the CE-4 surface in situ measurements of the visible and near-infrared spectrometer and the lunar penetrating radar (LPR) onboard Yutu-2 rover. To evaluate the sources and amounts of all principle foreign materials at the CE-4 landing site, we thoroughly examine the ejecta delivered by crater-forming events that occurred later than the formation of the mare basalts at the CE-4 landing site. We found a total of 16 craters that may have delivered ejecta thicker than 10 cm level superposed on the mare basalts at the CE-4 landing site. Crater Finsen, Von Kármán L, Von Kármán L′, and Maksutov are the top four major foreign material sources, and each of them contributed ejecta thicker than 1 m. Our surveys confirm that the ejecta from Finsen crater are the most dominant foreign materials in the uppermost few meters at the CE-4 landing site and the total impact ejecta deposited upon the mare basalts at the landing site is estimated to be thinner than 30 m. We found that the estimations from Pike's model are the most consistent with the Yutu-2 LPR observations.

Unified Astronomy Thesaurus concepts: The Moon (1692); Lunar craters (949)

1. Introduction

On 2019 January 3, China's Chang'e-4 (CE-4) lunar probe successfully landed in the Von Kármán crater on the lunar far side and deployed the Yutu-2 rover. The landing site (coordinated at 45.4446°S, 177.5991°E; Li et al. 2019) was later officially named as Statio Tianhe by the International Astronomical Union (IAU). Von Kármán is an impact crater with a diameter of ∼186 km and is located inside the heavily cratered South Pole–Aitken (SPA) basin (Figure 1), the largest and oldest known impact structure on the Moon (Spudis et al. 1994; Garrick-Bethell & Zuber 2009). Although Von Kármán is an ancient crater with a pre-Nectarian age (Losiak et al. 2009; Yingst et al. 2017), the crater floor was resurfaced by younger multiple-phase Imbrian-aged mare basalts (Yingst & Head 1997; Yingst et al. 2017; Pasckert et al. 2018). After those basalts were deposited, the impact ejecta of many postdated craters on the entire Moon successively superposed on these mare basalt units (termed "post-mare craters" in this study), creating the current geologic settings of the CE-4's landing site.

Understanding the origin and amounts of foreign materials at the CE-4 landing site is essential for analyzing the local stratigraphy and geologic history. Before the landing of CE-4, Huang et al. (2018) reported its landing site is mainly superposed by the ejecta from at least four nearby (all <140 km in distance from the landing site) craters: Finsen, Von Kármán L, Von Kármán L′, and Antoniadi. After the landing, the visible and near-infrared spectrometer (VNIS) onboard the Yutu-2 rover found that the mafic materials around the landing site are dominated by orthopyroxene, different from the clinopyroxene-dominated mare basalts. Some researchers (Huang et al. 2018; Hu et al. 2019; Li et al. 2019) suggested that these materials are likely originated from the nearby Finsen crater, a ∼73-km-diameter crater of the Eratosthenian period (Wilhelms & Byrne 2009; Fortezzo et al. 2020), since the landing site is crossed by ejecta rays from Finsen and the Finsen ejecta is also dominated by orthopyroxene. In addition, the lunar penetrating radar (LPR) onboard the Yutu-2 rover also suggests that the uppermost stratigraphy at the CE-4 landing site is a fine regolith layer underlain by several impact ejecta deposit layers, including that of Finsen crater (Lai et al. 2019; Li et al. 2020; Zhang et al. 2021a).

However, the foreign materials delivered from relatively distant sources have not yet been carefully surveyed and Finsen ejecta may not be the only principal source for the materials detected by the Yutu-2 rover. Therefore, it is important to carefully survey all the possible principal sources of these foreign materials on the Moon and evaluate their influence on the CE-4 landing site. Furthermore, various empirical ejecta distribution models have been widely used to estimate ejecta thickness in different studies (McGetchin et al. 1973; Pike 1974; Housen et al. 1983; Sharpton 2014), while few assessments and comparisons of these models have been conducted.

In this study, we examine all possible principal sources of foreign materials at the CE-4 landing site, quantitatively evaluate their contributions to the local stratigraphy, and analyze their effects on the in situ observations from the VNIS and LPR of the CE-4 probe. In addition, the ejecta thickness and local stratigraphy derived from different models are analyzed and compared in detail.

2. The Identification of Post-mare Craters for the CE-4 Landing Site

Prior crater counting analyses for different areas determined the ages of the Von Kármán mare units as 3.75–3.15 Ga

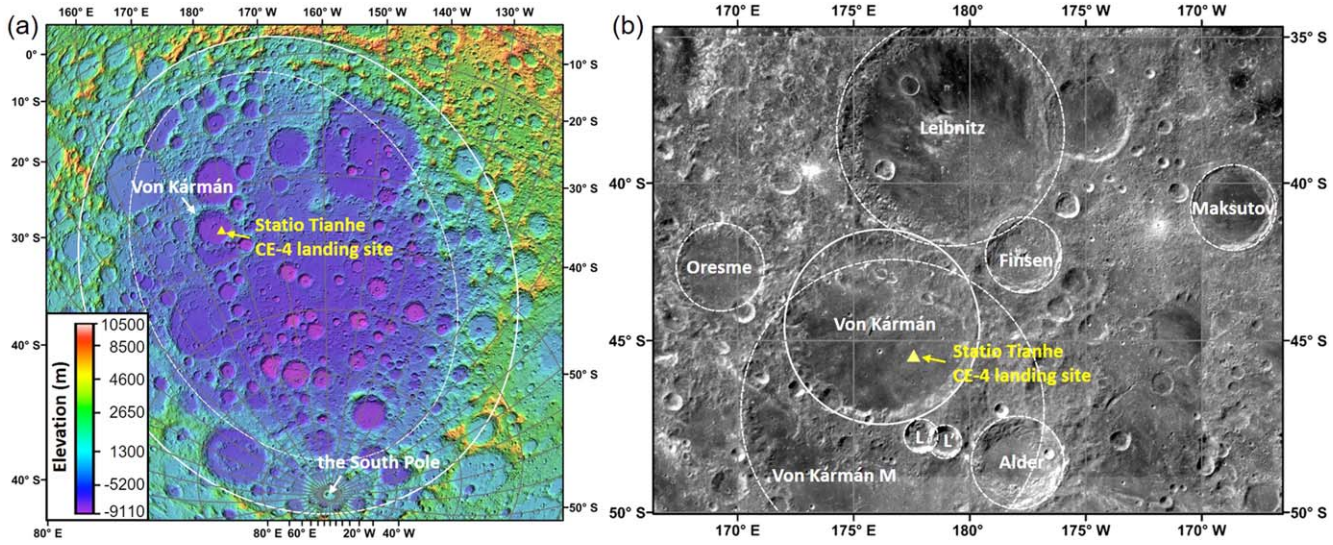


Figure 1. The location and surrounding context of Statio Tianhe, the Chang'e-4 (CE-4) landing site. (a) The topography of the CE-4 landing site within the Von Kármán crater shown on a Lunar Orbiter Laser Altimeter (LOLA) color-shaded relief map with a resolution of 128 pixels/degree. The white ovals mark the best-fit topographic inner ring and outer ellipse of the SPA basin according to Garrick-Bethell & Zuber (2009). The projection is orthographically centered on the SPA basin (53°S, 191°E). (b) The craters around Von Kármán crater shown on a CE-2 Digital Orthophoto Map (DOM) with a resolution of 7 m/pixel (IDs: J101, J102, J139, J140, J201, J202, J239, J240, K101, K102, K135, K136, K201, K202, K235, and K236). The solid and dashed circles show the size of the labeled craters according to Robbins (2019). Labels L and L′ represent the Von Kármán L and Von Kármán L′ craters, respectively. This map is shown in the Mercator projection centered on the Von Kármán crater (44.45°S, 176.25°E).

(Haruyama et al. 2009; Huang et al. 2018; Pasckert et al. 2018; Ling et al. 2019), roughly corresponding to the Late Imbrian Epoch (3.80–3.20 Ga; Stöffler & Ryder 2001). Therefore, we focus on craters contemporaneous with and younger than the Late Imbrian Epoch (i.e., "post-mare craters") throughout the surface of the Moon in this study.

The database of Robbins (2019) is used to obtain the sizes and locations of lunar craters. The stratigraphic ages of lunar craters and basins mainly refer to the most recent geologic map of Fortezzo et al. (2020), which is the first unified global lunar geologic map at a 1:5,000,000-scale. Cross-cutting and superposition relationships are also considered if the stratigraphy of the crater is not identified in the geologic map of Fortezzo et al. (2020). The Lunar Reconnaissance Orbiter Camera (LROC) Wide Angle Camera (WAC) mosaic image is used to evaluate the geologic context of these craters.

3. Models and Modifications

3.1. The Thickness of the Primary Ejecta

Multiple models were proposed to estimate the primary ejecta thickness $\delta(r)$ from an impact crater at a spherical distance r from the crater center:

1. Pike's model (Pike 1974):

$$\delta = 0.033R_t(r/R_t)^{-3.0}, \tag{1}$$

2. McGetchin's model (McGetchin et al. 1973):

$$\delta = 0.14{R_t}^{0.74}(r/R_t)^{-3.0}(\text{in m}), \tag{2}$$

3. Housen's model (Housen et al. 1983):

$$\left(\frac{\delta}{R_{\text{at}}}\right) = \frac{A_1(e_r-2)}{2\pi}(\sin 2\theta)^{e_r-2}\, r^{*-e_r} \times\left[1+\frac{4e_r-5}{3}\left(\frac{r^*}{\sin 2\theta}\right)^{-(e_r-2)/2}\frac{A_2}{r^*}\right] \text{ (in the gravity regime)}, \tag{3}$$

and (4) Sharpton's model (Sharpton 2014):

$$\delta = \begin{cases} 0.014R^{1.01}(r/R)^{-3} & \text{for simple crater} \\ 3.95R^{0.399}(r/R)^{-3} & \text{for complex crater} \end{cases} \text{(in m)}, \tag{4}$$

where R_t is the transient rim radius of the crater, R_{at} is the apparent transient radius at the surface, $r^* = \frac{r}{R_{\text{at}}}$ is the nondimensional distance from the crater center, and R is the final rim radius of the crater. The transient radius at the surface R_{at} is approximately 83% of the transient rim radius R_t (Baldwin 1963; Pike 1974). For Housen's model (Equation (3)), θ is the ejecta launch angle, $A_1 = 0.2$ is constant, and A_2 and e_r are target property-related parameters (Housen et al. 1983). By adopting the typical impact angle of $\theta = 45°$ and widely used target parameters($A_2 = 0.82$, $e_r = 2.61$) for Ottawa sand, Equation (3) can be simplified as (Xu & Xie 2020):

$$\delta = 0.0100 \times R_t\left(\frac{r}{R_t}\right)^{-2.6145} + 0.011724 \times R_t\left(\frac{r}{R_t}\right)^{-3.9217} \tag{5}$$

noting that the ejecta thickness δ estimated from Housen's model is highly determined by the specific ejection angle and target property, which will be further discussed in Section 4.2.

In addition, if the distance between the center of the impact crater and the ejecta delivery area is considerably large, the distances of the ejecta after ballistic trajectories are not great-circle distances and the ejecta cannot be treated simply as being deposited on a flat surface. Therefore, two kinds of correction should be taken into consideration: (1) distance correction and (2) deposition correction. We use the improved ballistic sedimentation model of Haskin et al. (2003) and Xie et al. (2020a) in this section. This method assumes that the ejecta launched from each impact crater is symmetric and the ejecta

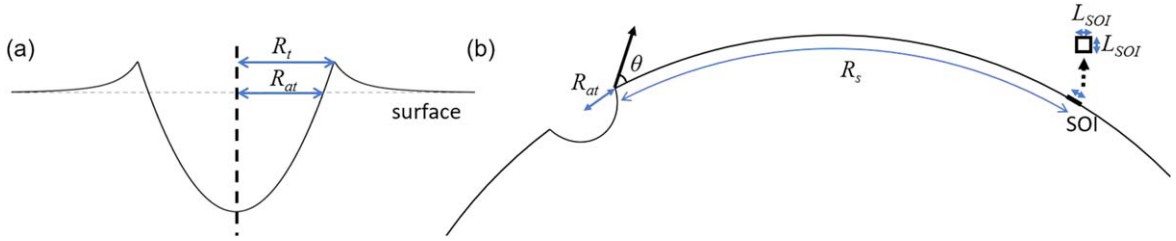


Figure 2. (a) Schematic showing the rim radius, $\boldsymbol{R_t}$, and the apparent radius, $\boldsymbol{R_{at}}$ (i.e., the radius at the surface), of a transient cavity. (b) Side view showing a primary transient crater, the launch angle θ and the travel distance $\boldsymbol{R_s}$ of the ejecta, and the location and size, $\boldsymbol{LSOI}$, of the SOI.

emplacements are not affected by the pre-existing topography, as with previous models (Section 3.1).

3.1.1. The Distance Correction

For simplicity, we assume that primary ejecta from an impact crater with a final rim radius of R is launched from the transient cavity radius at the surface R_{at}, with a velocity of $v(R_S)$ and an ejection angle of θ measured from the horizon, and falls on a square of interest (SOI) with a length of $L_{SOI} = \frac{1}{4}R_{at}$ after a ballistic trajectory, as shown in Figure 2.

We consider $R_t = 0.84R$ for simple craters (Melosh 1989) and $R_t = R_{SC}^{0.15}R^{0.85}$ for complex craters (Croft 1985), where $R_{SC} = 9.5$ km is the transition radius from simple to complex craters (Pike 1980).

In addition, considering that R_{at} is generally substantially smaller than the average radius $R_0 = 1737.1$ km of the Moon, the arc distance from the center of the impact crater to the location of R_{at} can be treated as approximately equal to R_{at}. Therefore, the spherical distance from the launch point to the ejecta delivery area SOI, is:

$$R_S \approx d_{\text{sphere}} - R_{at} \tag{6}$$

where d_{sphere} is the spherical distance from the center of the crater to the SOI region.

The velocity of the primary ejecta (Melosh 1989, p. 87; Haskin et al. 2003, Equation (9)) is:

$$v(R_s) = \frac{\sqrt{R_0 g \tan X}}{\sqrt{\tan X \cos^2\theta + \sin\theta\cos\theta}} \tag{7}$$

where g is the surface gravity of the Moon and $X = R_S/(2R_0)$.

The actual distance of the ejecta is:

$$r(R_s) = R_{at} + \frac{v^2(R_s)\sin(2\theta)}{g}. \tag{8}$$

Assuming the typical ejection angle of $\theta = 45°$ and substituting Equation (7) into Equation (8), Equation (8) can be further simplified to:

$$r(R_s) = R_{at} + \frac{2R_0\tan X}{\tan X + 1} \tag{9}$$

noting that the revised distance, $r(R_s)$, is irrespective of the value of surface gravity, g.

3.1.2. The Deposition Correction

For the region of a SOI with a radical length of $L_{SOI} = \frac{1}{4}R_{at}$, as shown in Figure 2(b), the inner and outer boundaries from the center of the primary crater are $r_{\text{inner}} = r(d_{\text{sphere}} - L_{SOI}/2)$ and $r_{\text{outer}} = r(d_{\text{sphere}} + L_{SOI}/2)$, respectively. Considering that ejecta thickness decreases as a power function with distance, the average thickness of the emplaced ejecta within the SOI is approximately equal to the thickness at the geometry mean distance at $\bar{r} = \sqrt{r_{\text{inner}} r_{\text{outer}}}$.

Combining the above terms with Equations (1)–(4), the primary ejecta thickness at the SOI region, δ_{SOI}, can be derived as:

$$\delta_{SOI} = \frac{S_{\text{ring_flat}}}{S_{\text{ring}}}\delta(\bar{r}) \tag{10}$$

where $S_{\text{ring}} = 2\pi R_0^2(\cos((d_{\text{sphere}} - L_{SOI}/2)/R_0) - \cos((d_{\text{sphere}} + L_{SOI}/2)/R_0))$ is the area of a ring for a spherical planetary body and $S_{\text{ring_flat}} = \pi(r_{\text{outer}}^2 - r_{\text{inner}}^2)$ is the area of a ring emplaced on a flat surface.

3.2. The Depth of Local Materials

The local ejecta stratigraphy is determined not only by the amount of primary ejecta but also by the degree of mixing of the primary ejecta and the local materials excavated by the ejecta. Taking the mixing model of Petro & Pieters (2004, 2006, 2008), which is modified from the initial model of Oberbeck et al. (1975), the ratio, μ', of the thickness of the local materials to the primary ejecta can be estimated by:

$$\mu' = \begin{cases} \mu, & \mu \leqslant 5 \\ \mu/2 + 2.5, & \mu > 5 \end{cases}$$
$$\text{and } \mu = 0.0183r^{0.87} \text{ (in km)}. \tag{11}$$

4. Evaluating the Amounts of Ejecta Materials On the Mare Basalts at the Chang'e-4 Landing Site

For our estimations, the lower threshold of the ejecta thickness is based on the vertical resolution of the Yutu-2 LPR, which is no less than 15 cm for the high-frequency channel and greater than 1 m for the low frequency channel (Lai et al. 2019, 2020). Therefore, we take 10 cm as the threshold and consider that only the ejecta estimated to be thicker than 10 cm level are potentially distinguished from LPR observations. However, we should note that the modeled thickness of distal ejecta beyond continuous ejecta blankets may be of high uncertainty, so we only use this threshold as a rough lower limit. All four models, Pike (1974), McGetchin et al. (1973), Housen et al. (1983), and Sharpton (2014), are used for thickness estimations in this study, and we only survey the craters that delivered primary ejecta thicker than the threshold based on the maximum values among these four models.

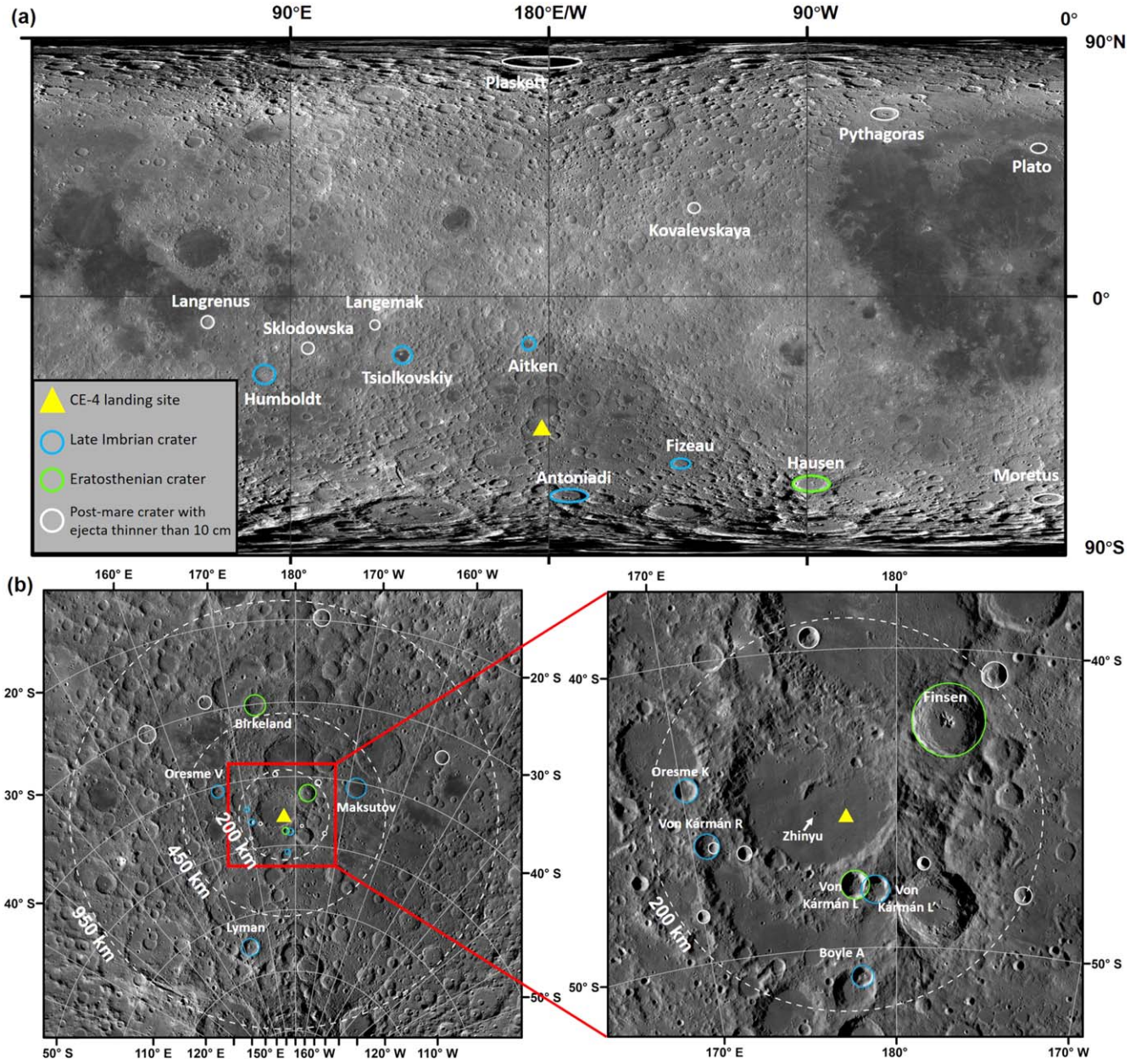


Figure 3. Locations of all post-mare craters identified in this study: (a) craters with $D \geqslant 100$ km (simple cylindrical projection) and (b) craters with $D < 100$ km (stereographic projection center at the CE-4 landing site). The base image is a LROC WAC mosaic image. The dashed white circles in (b) mark the examined boundaries of spherical distances of 950, 450, and 200 km from the CE-4 landing site. The colored craters are the post-mare craters that delivered ejecta >10 cm in thickness to the mare units at the CE-4 landing site (Late Imbrian craters are in cyan and Eratosthenian craters are in green), and the white craters are the post-mare craters that delivered ejecta <10 cm in thickness. The yellow triangle marks the location of the CE-4 landing site.

4.1. Possible Sources of Foreign Materials at the CE-4 Landing Site

4.1.1. Thickness of Primary Ejecta from Large Post-mare Craters (D ⩾ 100 km)

Since the larger impact cratering events can produce larger craters and deliver more ejecta to other locations (assuming the other factors are the same), we first surveyed the thickness of large craters' ($D \geqslant 100$ km) primary ejecta present at the CE-4 landing site in this subsection.

According to the geologic ages summarized by the geologic map of Fortezzo et al. (2020), there are a total of 14 impact craters larger than 100 km throughout the surface of the Moon within or younger than the Late Imbrian Epoch (Figure 3(a) and Table 1). Among them, six craters (Hausen, Humboldt, Tsiolkovskiy, Antoniadi, Aitken, and Fizeau) contributed ejecta >10 cm in thickness to the CE-4 landing site according to Pike's model (the model that predicts the maximum ejecta thickness, as referred in the sections below).

According to Pike's model (Table 1), most of the ejecta from the large post-mare craters ($D \geqslant 100$ km) to the CE-4 landing site is from Antoniadi crater of the Late Imbrian Epoch, with an ejecta thickness of 57 cm. The Hausen crater is the only Eratosthenian-aged crater that contributed considerable amounts of ejecta, with a thickness of 13 cm. All large post-mare craters ($D \geqslant 100$ km) on the Moon considered in this

Table 1
All Post-mare Craters that Contributed Ejecta >10 cm in Thickness and the Thickness of their Ejecta at the CE-4 Landing Site[a]

Crater	Stratigraphy (Fortezzo et al. 2020)[b]	Diameter (km)	Longitude (°)	Latitude (°)	Spherical Distance (km)	Ejecta Thickness (m)			
						Pike's model	McGetchin's model	Housen's Model	Shapton's model
Humboldt	Ic2	204.25	80.96	−27.18	2283.3	0.11	0.03	0.11	0.05
Tsiolkovskiy	Ic2	183.71	129.05	−20.38	1421.4	0.24	0.06	0.22	0.12
Antoniadi	Ic2	137.89	−172.99	−69.40	739.9	0.57	0.15	0.48	0.28
Aitken	Ic2	132.98	173.05	−16.50	885.6	0.30	0.08	0.27	0.15
Fizeau	Ic2	106.79	−134.08	−58.21	958.8	0.11	0.03	0.11	0.06
Lyman	Ic2	84.60	162.47	−64.96	642.7	0.17	0.05	0.15	0.08
Maksutov	Ic2	84.53	191.36	−40.79	335.4	**1.13**	**0.32**	**0.86**	**0.55**
Oresme V	Ic2	53.98	165.41	−40.70	305.4	0.33	0.10	0.27	0.16
Von Kármán L′ [c]	Ic2	29.04	178.93	−48.00	82.0	**2.06**	**0.73**	**1.38**	**1.00**
Von Kármán R	Ic2	25.44	170.76	−46.04	145.6	0.23	0.09	0.19	0.11
Oresme K	Ic2	23.52	170.21	−44.09	164.0	0.13	0.05	0.11	0.06
Boyle A	Ic2	22.97	178.14	−51.00	168.3	0.11	0.04	0.09	0.05
Total ejecta thickness of Late Imbrian craters						5.5	1.7	4.2	2.7
Hausen	Ec	165.01	−88.57	-65.20	1550.8	0.13	0.03	0.13	0.06
Birkeland	Ec	81.65	173.99	−30.16	471.6	0.37	0.10	0.31	0.18
Finsen	Ec	73.10	182.31	−42.32	140.4	**9.39**	**2.73**	**5.94**	**4.57**
Von Kármán L	Ec	29.65	177.90	−47.83	72.2	**3.22**	**1.14**	**2.09**	**1.57**
Total ejecta thickness of Eratosthenian craters						13.1	4.0	8.5	6.4
Total ejecta thickness for all large post-mare craters ($D \geqslant 100$ km)						1.5	0.4	1.3	0.7
Total ejecta thickness for all small post-mare craters ($D < 100$ km)						17.1	5.4	11.4	8.3
Total ejecta thickness for all post-mare craters						18.6	5.7	12.7	9.0

Notes.
[a] The crater sizes and locations are according to the crater database of Robbins (2019) and the values marked in bold font show the four thickest ejecta.
[b] Ic2 indicates Late Imbrian craters, and Ec indicates Eratosthenian craters.
[c] We provisionally use the name of Von Kármán L′ according to Huang et al. (2018), which is not an IAU-approved name.

study delivered a total ejecta thickness of 1.5 m at the CE-4 landing site.

4.1.2. Thickness of Ejecta from Small Post-mare Craters (D < 100 km)

For any lunar post-mare crater ($D < 100$ km) beyond a spherical distance of 950 km from the CE-4 landing site, the maximum thickness of its ejecta on the mare basalts at the CE-4 landing site is ∼9 cm (i.e., within the threshold of 10 cm in this study; based on Pike's model). Therefore, we can narrow the examination range in this study. Similarly, for any impact crater smaller than 50 km in diameter and beyond a spherical distance of 450 km from the CE-4 landing site, and for any impact crater smaller than 25 km in diameter and beyond a spherical distance of 200 km, the upper limits of ejecta thickness were estimated to be ∼8 cm and ∼9 cm, respectively, which are considered neglectable (<10 cm in thickness) in this study. Within the range of a spherical distance of 200 km from the CE-4 landing site, there are no smaller post-mare craters ($D < 10$ km) nearby that could deliver ejecta >10 cm in thickness based on our observations and calculations (Figure 3(b)). For example, the Copernican crater Zhinyu (with a diameter of 3.75 km located ∼30 km from the landing site; Figure 3(b)) delivered ejecta with a thickness less than 2 cm (from the four models in Section 3) superposed on the CE-4 landing site. Therefore, we exclude the contributions from craters with $D < 10$ km in this study. In summary, we examine post-mare craters in the following order: (1) 50 km $\leqslant D < 100$ km within a spherical distance of 950 km, (2) 25 km $\leqslant D < 50$ km within a spherical distance of 450 km, and (3) 10 km $\leqslant D < 25$ km within a spherical distance of 200 km from the CE-4 landing site in this section.

We find a total of 10 small post-mare craters ($D < 100$ km) that contributed ejecta >10 cm in thickness to the CE-4 landing site based on Pike's model, as shown in Figure 3(b) and listed in Table 1.

Based on Pike's model, all these identified small post-mare craters ($D < 100$ km) delivered a total ejecta thickness of ∼17.1 m upon the CE-4 landing site. Among them, the Eratosthenian crater Finsen contributed the most ejecta (∼9.4 m), followed by the Eratosthenian crater Von Kármán L (∼3.2 m) and the Late Imbrian crater Von Kármán L′ (∼2.1 m). Taking the most dominant contributor (Finsen crater) as the boundary, all these small craters ($D < 100$ km) formed earlier than Finsen crater (i.e., they delivered ejecta deposited below the Finsen ejecta) and contributed a total ejecta thickness of ∼5.5 m (Table 1).

4.2. Comparisons of Primary Ejecta Thicknesses between the Four Ejecta Models

All 16 post-mare craters, including the large ($D \geqslant 100$ km) and small ($D < 100$ km) craters identified in this study, delivered total primary thicknesses of 18.6, 5.7, 12.7, and 9.0 m at the CE-4 landing site based on the ejecta models of Pike (1974), McGetchin et al. (1973), Housen et al. (1983), and Sharpton (2014), respectively (Table 1).

Pike's model gives the largest thickness estimates among the four models as shown in Table 1. For the same identified craters, primary ejecta thicknesses derived from McGetchin's model and Shapton's model are only $\sim 1/3$ and $\sim 1/2$ of those from Pike's model, respectively. This indicates that the ejecta thicknesses estimated from these three models are roughly proportional to the same exponential term of $(r/R_t)^{-3.0}$ (Equations (1), (2), and (4)).

Pike's and McGetchin's models are derived from the same observation data sets (McGetchin et al. 1973; Pike 1974), and their discrepancy is due to the fact that Pike's model excluded two obviously unreliable data points (i.e., Copernicus crater and Imbrium basin). In this respect, Pike's model may provide more reliable estimations than McGetchin's model, which is also supported by recent studies (e.g., Xie & Zhu 2016; Xu & Xie 2020).

Both Sharpton's and Pike's model comes from actual ejecta measurements, their discrepancy is possibly due to two aspects: (1) Sharpton's model underestimates the ejecta thickness by a factor of ~ 2 or Pike's model overestimates the ejecta thickness by a factor of ~ 2 (Sharpton's model itself has a measurement uncertainty of $\sim \pm 30\%$; Sharpton 2014); (2) the inversion relationship from the final radius to the transient radius derived by Croft (1985) is unsuitable for the craters identified in this study, resulting in larger transient radiuses for Pike's model (and also for MacGetchin and Housen's models) and thus thicker ejecta.

The discrepancy between Housen's model and another three models is more complicated. The ejecta thickness estimated from Housen's model is highly determined by the specific ejection angle (θ) and target property (A_2 and e_r) but, in reality, those parameters may be varied for each specific impact event and ejecta deposition process. In this study, we use the typical ejection angle of $\theta = 45°$ and widely used target parameters ($A_2 = 0.82$, $e_r = 2.61$) for Ottawa sand and, if the estimated thickness and the actual thickness are inconsistent, the inconsistency is more likely due to that the choice of those parameters may be not suitable for the specific case at the CE-4 landing site, rather than the model validation itself. For example, if the ejection angle varies within $\pm 20\%$ from the typical value (i.e., $\boldsymbol{\theta}$ varies from 36°–54°), the ejecta thickness will decrease $<3\%$ compared with the current result for the case of Finsen's ejecta to the CE-4 landing site. Similarly, if the target parameters A_2 or e_r vary within $\pm 20\%$ from the typical value, the ejecta thickness will vary within $\pm 3\%$ and decrease $<64\%$ compared with the current result, respectively. Therefore, we must note that the ejecta thicknesses derived from Housen's model are insensitive to the minor variations from the typical values of parameters $\boldsymbol{\theta}$ and A_2 used in this study, but sensitive to the variations of target parameter e_r.

In addition, ejecta thicknesses estimated from Housen's model have different trends for near and distant craters. For most distant craters (beyond $\sim 5\ R_t$; Table 1), Housen's model gives similar ejecta estimates compared to those of Pike, while for a few nearer craters (Finsen, Von Kármán L, Von Kármán L′, and Maksutov; all within $\sim 5\ R_t$), their ejecta thicknesses derived from Housen's model are $\sim 2/3$ of those from Pike's model. This is because that for the nearer craters, both the terms $(r/R_t)^{-2.6145}$ and $(r/R_t)^{-3.9217}$ in Equation (3) play important roles in the thickness estimations, while for distance craters, only the low-order term $(r/R_t)^{-2.6145}$ plays an important role.

4.3. The Principal Contributors of Foreign Materials at the CE-4 Landing Site

The first five lunar days of Yutu-2 LPR observations show that the uppermost stratigraphy upon the local basalts at the CE-4 landing site have four obvious reflectors (Lai et al. 2019) that may correspond to various ejecta layers from four main impact events. Therefore, we find the craters delivering the top four thick ejecta to the CE-4 landing site as the principal contributors: (1) Finsen crater of the Eratosthenian Period ($\sim$9.4 m; based on Pike's model; similarly hereinafter), (2) Von Kármán L crater of the Eratosthenian Period ($\sim$3.2 m), (3) Von Kármán L′ crater of the Late Imbrian Epoch ($\sim$2.1 m), and (4) Maksutov crater of the Late Imbrian Epoch ($\sim$1.1 m). This differs slightly from the results of Huang et al. (2018) in that the ejecta from Maksutov crater outweighing Antoniadi crater (also a Late Imbrian crater contributing an ejecta 57 cm thick) plays a more important role than previously thought (Huang et al. 2018).

Because the ratio, μ', is only determined by the distance, r, between the center of the impact crater and the ejecta destination, the ratio of the thickness of local materials to the primary ejecta is irrelevant to the choice of ejecta models. Therefore, Finsen crater caused the thickest local materials and thus the thickest mixing zones (i.e., ejecta deposits, which are the combination of primary ejecta and local materials) at the CE-4 landing site, followed by Von Kármán L and Maksutov craters, regardless of the ejecta models, as shown in Table 2.

5. Discussion

5.1. The Emplacement Sequence of these Principal Ejecta at the CE-4 Landing Site

For simplicity, we only discuss the emplacement sequence of the top four principal source craters (Table 2). Although, according to Fortezzo et al. (2020), the two Eratosthenian craters Finsen and Von Kármán L formed later than the two Late Imbrian craters Von Kármán L′ and Maksutov, the relative age between the two craters in the same period is unknown and it is impractical to directly compare the absolute model ages of these four craters by crater counting because the countable areas of Von Kármán L and Von Kármán L′ craters are too small.

The Diviner rock abundance (RA; Bandfield et al. 2011) of crater ejecta shows an inverse correlation with crater age (Ghent et al. 2014). Because the Diviner-derived RA around Finsen crater is higher than that around Von Kármán L crater (Figure 4), we consider Finsen crater to be younger than Von Kármán L crater. However, since the RA around crater Maksutov and Von Kármán L′ are low and difficult to compare, it is impractical to deduce the relative ages of these two craters by using this method. Instead, we refer to the

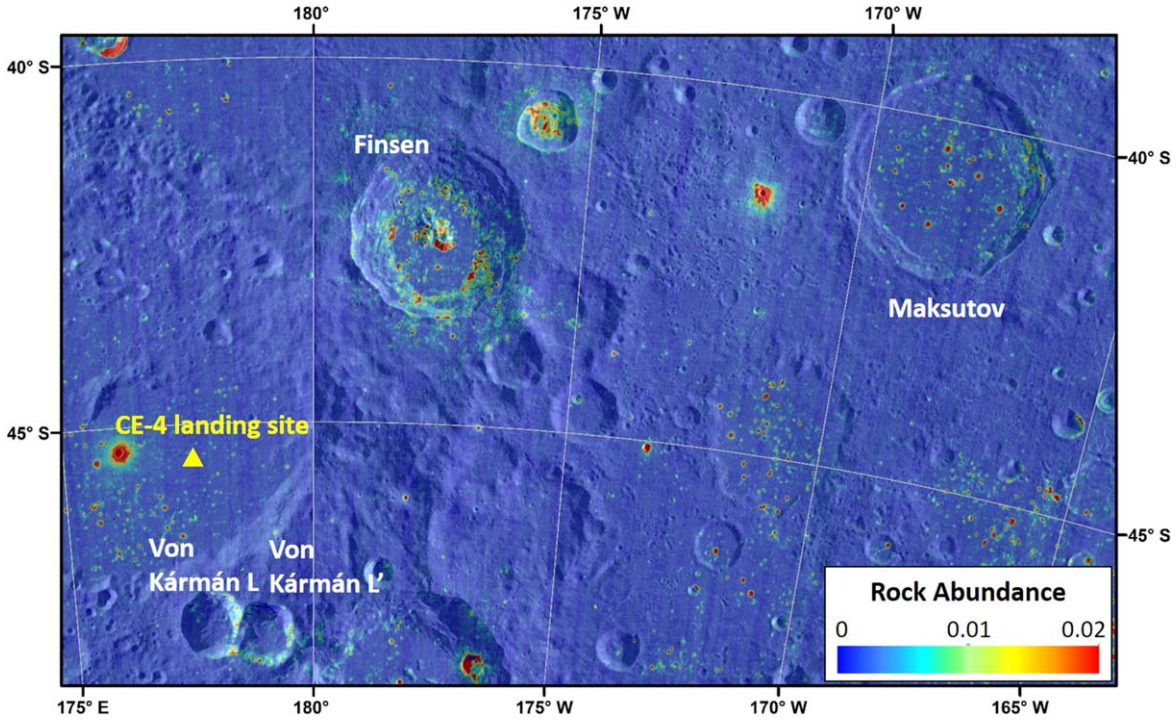


Figure 4. Diviner-derived rock abundance (Bandfield et al. 2011) around Finsen, Von Kármán L, Von Kármán L′, and Maksutov craters. This map is shown in the Mercator projection centered on Von Kármán crater.

Table 2
The Thickness of Local Materials and Ejecta Deposits of All Post-mare Craters Contributing Ejecta >10 cm in Thickness to the CE-4 Landing Site[a]

Crater	Ratio of Primary Ejecta[b]	Pike's Model (m)		McGetchin's Model (m)		Housen's Model (m)		Shapton's Model (m)	
		Local Materials	Ejecta Deposits[c]	Local Materials	Ejecta Deposits	Local Materials	Ejecta Deposits	Local Materials	Ejecta Deposits
Humboldt	0.09	1.12	1.23	0.26	0.29	1.13	1.24	0.54	0.60
Tsiolkovskiy	0.12	1.82	2.07	0.43	0.49	1.67	1.90	0.89	1.00
Antoniadi	0.16	3.08	3.65	0.78	0.92	2.56	3.04	1.50	1.77
Aitken	0.15	1.77	2.07	0.45	0.53	1.56	1.83	0.86	1.00
Fizeau	0.14	0.70	0.81	0.19	0.22	0.67	0.78	0.34	0.39
Lyman	0.17	0.83	1.00	0.24	0.28	0.77	0.92	0.41	0.49
Maksutov	**0.26**	**3.27**	**4.40**	**0.92**	**1.24**	**2.48**	**3.34**	**1.59**	**2.14**
Oresme V	0.27	0.87	1.20	0.27	0.37	0.72	1.00	0.42	0.58
Von Kármán L′	**0.54**	**1.74**	**3.80**	**0.62**	**1.36**	**1.17**	**2.54**	**0.85**	**1.85**
Von Kármán R	0.42	0.33	0.56	0.12	0.21	0.27	0.46	0.16	0.27
Oresme K	0.39	0.19	0.32	0.07	0.12	0.17	0.28	0.09	0.16
Boyle A	0.39	0.17	0.28	0.06	0.10	0.15	0.24	0.08	0.13
Hausen	0.11	1.06	1.20	0.26	0.29	1.03	1.16	0.52	0.58
Birkeland	0.21	1.42	1.78	0.40	0.51	1.20	1.51	0.69	0.87
Finsen	**0.43**	**12.69**	**22.08**	**3.69**	**6.43**	**8.02**	**13.96**	**6.17**	**10.74**
Von Kármán L	**0.57**	**2.44**	**5.66**	**0.87**	**2.01**	**1.58**	**3.67**	**1.19**	**2.76**

Notes.
[a] The crater sizes and locations are according to the crater database of Robbins (2019) and the values marked in bold font show top four primary ejecta in Table 1.
[b] The ratios of primary ejecta to ejecta deposits are computed by $1/(1+\mu')$.
[c] Ejecta deposits are the sum of primary ejecta and local materials.

geologic map of Stuart-Alexander (1978) and obtain that Maksutov crater is older than Von Kármán L′ crater.

Given the above discussions, the most likely emplacement sequence of these four craters' ejecta at the CE-4 landing site (from oldest to youngest) is Maksutov, Von Kármán L′, Von Kármán L, and Finsen (scenarios of Figures 5 and 6).

5.2. The Stratigraphic Structure at the CE-4 Landing Site

If there is no local material excavation or mixing during each ejecta emplacement and no regolith production processes afterwards, these foreign materials from the four principal craters ought to be deposited as discrete layers in sequence, as

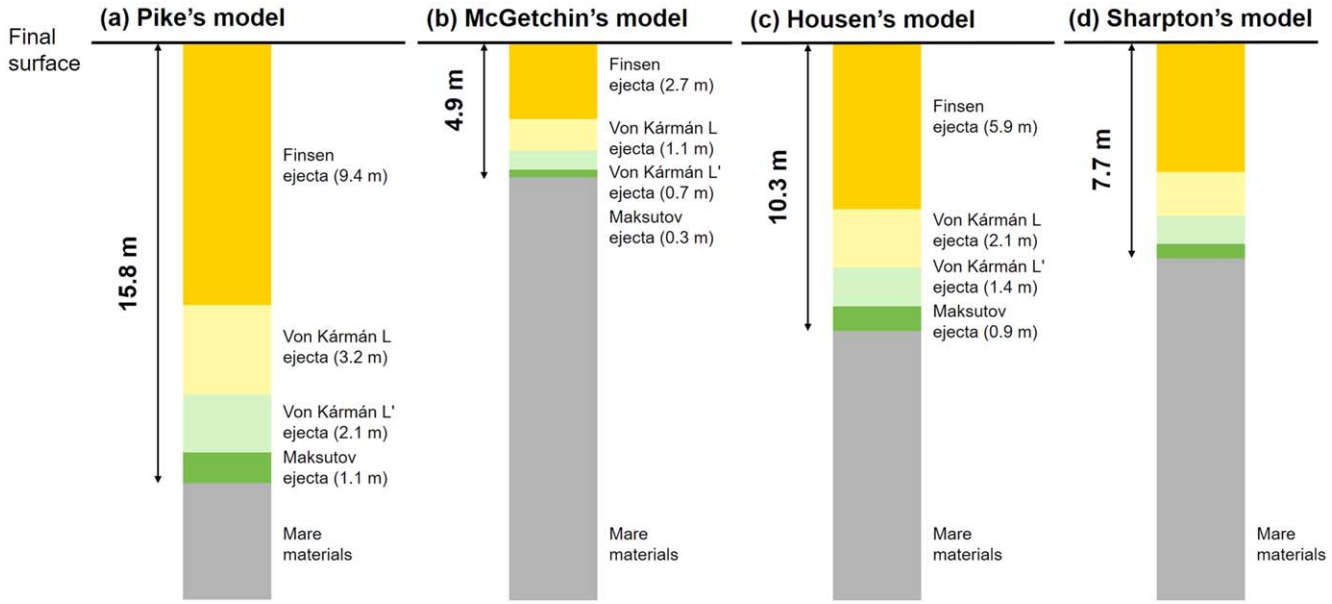


Figure 5. The emplacement stratigraphy at the CE-4 landing site without the consideration of local mixing and regolith production. (a)–(d) Ejecta thickness estimated from the four models with a sequence of older (bottom) to younger (top) of ejecta: from Maksutov, Von Kármán L′, Von Kármán L, and Finsen craters.

shown in Figure 5. In these scenarios, the Finsen ejecta should be the topmost layer among the four craters' ejecta with depths of ∼9.4 m, 2.7 m, 5.9 m, and 4.6 m based on the ejecta models of Pike (1974), McGetchin et al. (1973), Housen et al. (1983), and Sharpton (2014), respectively.

However, the final stratigraphic structure is not only determined by the primary ballistically deposited ejecta but also by the excavated local materials mixed with the ejecta. Therefore, the final stratigraphic layers reflect the mixture of the primary ejecta and the excavated local materials (i.e., ejecta deposits).

The endmember scenario is that the foreign materials mixed homogenously with the local materials (i.e., a mixing zone homogenously combined of primary ejecta and local materials). If so, the stratigraphic sequence should be much different from Figure 5. As time passed, each crater's ejecta would have emplaced atop the previously deposited ejecta sequentially, excavated previous local materials, and mixed with them. The stratigraphy after homogenous mixture processes is shown in Figure 6. Taking Figure 6(a) as an example: (1) first, the Maksutov impact delivered ejecta with a thickness of 1.1 m and excavated local materials (local mare basalts) with a thickness of 3.3 m, creating a 4.4 m-thick mixing zone with 26% of materials from Maksutov crater and 74% from local mare basalts. (2) Then, the Von Kármán L′ impact delivered ejecta with a thickness of 2.1 m and excavated local materials (mixture of local mare basalts and Maksutov ejecta) with a thickness of 1.7 m, creating a 3.8 m-thick mixing zone with 54% of materials from Von Kármán L′ crater and 46% of materials from the previous mixture (i.e., Maksutov ejecta and local mare basalts). Because the excavating depth of the Von Kármán L′ ejecta (1.7 m) is shallower than the previously created mixing zone (4.4 m), a 2.7 m-thick pre-existing mixing zone remains. (3) Similarly, the Von Kármán L impact delivered ejecta with a thickness of 3.2 m and excavated local materials (mixture of the local mare basalts and the ejecta from Von Kármán L′ and Maksutov) with a thickness of 2.4 m, creating a 5.7 m-thick mixing zone with 57% of materials from Von Kármán L and leaving two previous mixing zones. (4) The Finsen impact delivered ejecta with a thickness of 9.4 m and excavated local materials (mixture of local mare basalts and the ejecta from Von Kármán L, Von Kármán L′, and Maksutov) with a thickness of 12.7 m, creating a 22.1 m-thick mixing zone with 43% of materials from Finsen, but the two previous mixing zones were also mixed by the deep excavated local materials. As a result, previous layers of mixing zones produced by Maksutov, Von Kármán L′, and Von Kármán L would have been totally excavated by and mixed with the Finsen ejecta due to its sufficiently large excavation depth, regardless of the thickness models considered in this study.

The mixture process produced a total thickness of 22.1 m (Figure 6(a)), 6.4 m (Figure 6(b)), 14.0 m (Figure 6(c)), and 10.7 m (Figure 6(d)) based on the ejecta model of Pike (1974), McGetchin et al. (1973), Housen et al. (1983), and Sharpton (2014), respectively, including the primary ejecta and local materials of each ejecta-delivering event. Taking the ejecta deposits of all post-mare craters (Tables 1 and 2) into consideration, the impact ejecta upon the mare basalts at the CE-4 landing site ought to be no thicker than 30 m based on the maximum value (Pike' s model).

After the emplacement of Finsen ejecta, regolith production processes would further excavate and mix the near surface materials, making a fine-grained regolith layer with a proportion of Finsen ejecta remaining if the regolith is thinner than the topmost mixing zone (Figure 6). The actual regolith thickness can be determined from other methods, such as LPR (e.g., Lai et al. 2019; Li et al. 2019; Zhang et al. 2021a) or crater morphology (e.g., Quaide & Oberbeck 1968; Bart et al. 2011; Fa et al. 2014). As a result, the topmost layer at the CE-4 landing site ought to be a homogenously mixed regolith layer containing all previously deposited materials and a considerable amount of pre-existing local mare materials. The most abundant surface materials are Finsen ejecta (43%) if the regolith layer is thinner than the ejecta mixing layer of Finsen.

The true mixture scenario should be located between the two endmember scenarios of no mixing (Figure 5) and homogenous mixing (Figure 6). More specifically, the degree of mixing will decrease with increasing depth (Xie et al. 2020b). However, as

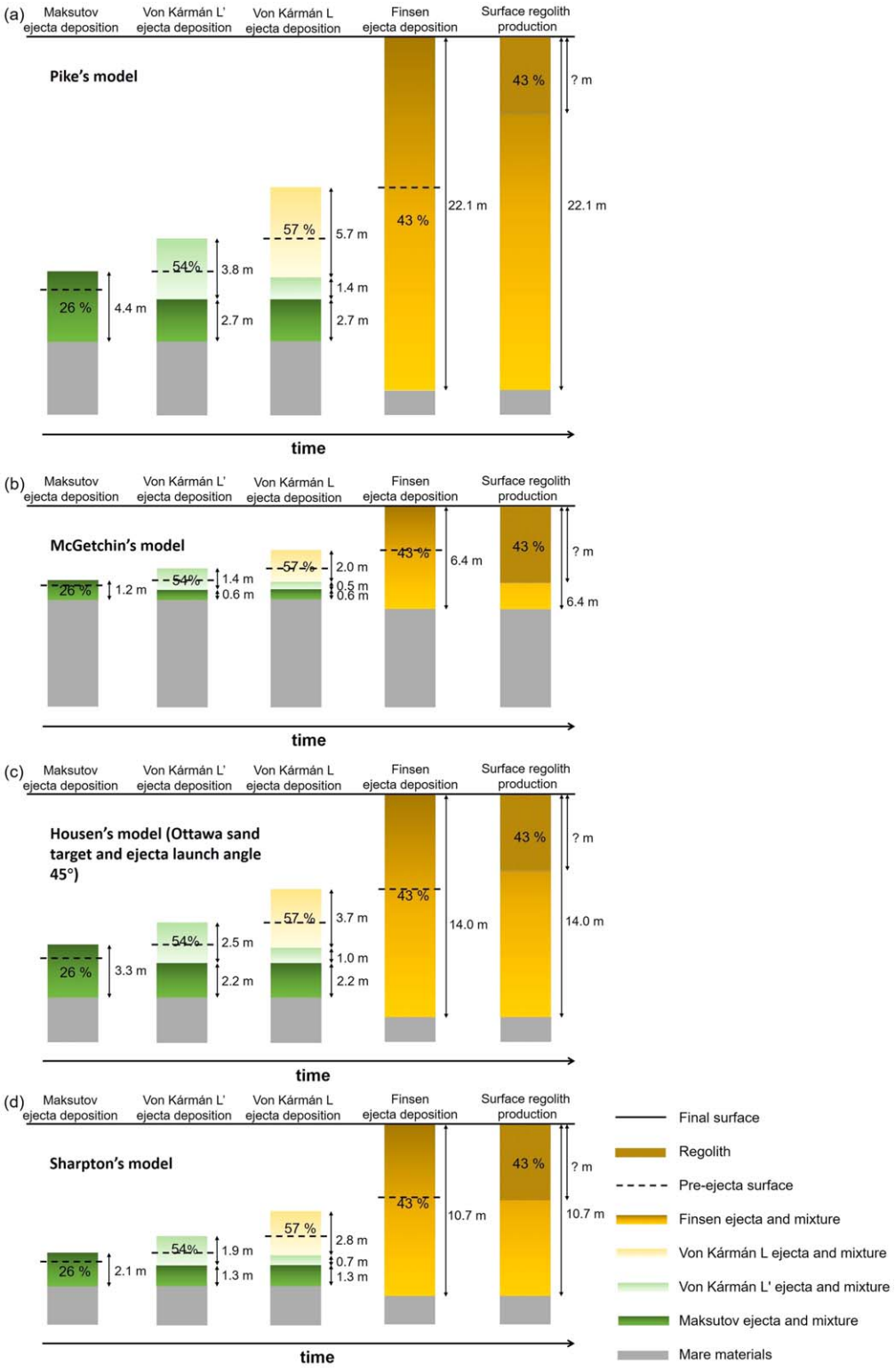


Figure 6. Illustration of the homogeneous mixing scenario showing the evolution of the stratigraphy with time at the CE-4 landing site. The mixture processes are illustrated under different emplacement orders ((a)–(d) for the ejecta sequence of Maksutov, Von Kármán L′, Von Kármán L, and Finsen, from older to younger) and thickness models (a for Pike's mode, b for McGetchin's model, c for Housen's model, and d for Sharpton's model). The percentage values are the percentage of the foreign materials at the topmost layer and the regolith thickness can be determined by other methods.

long as the regolith layer is thinner than the ejecta deposits of Finsen, the Finsen ejecta ought to be the most dominant material (with a ratio of at least 43%) from the surface to several meters deep at the CE-4 landing site. This is consistent with the spectral analysis of the Yutu-2 VNIS observations that the regolith at the CE-4 landing site is dominated by non-mare materials, and that its composition is similar to the Finsen ejecta (Huang et al. 2018; Hu et al. 2019). Note that, according to Zhang et al. (2021b), the large craters and basins in the SPA region should penetrate the orthopyroxene-rich materials of the

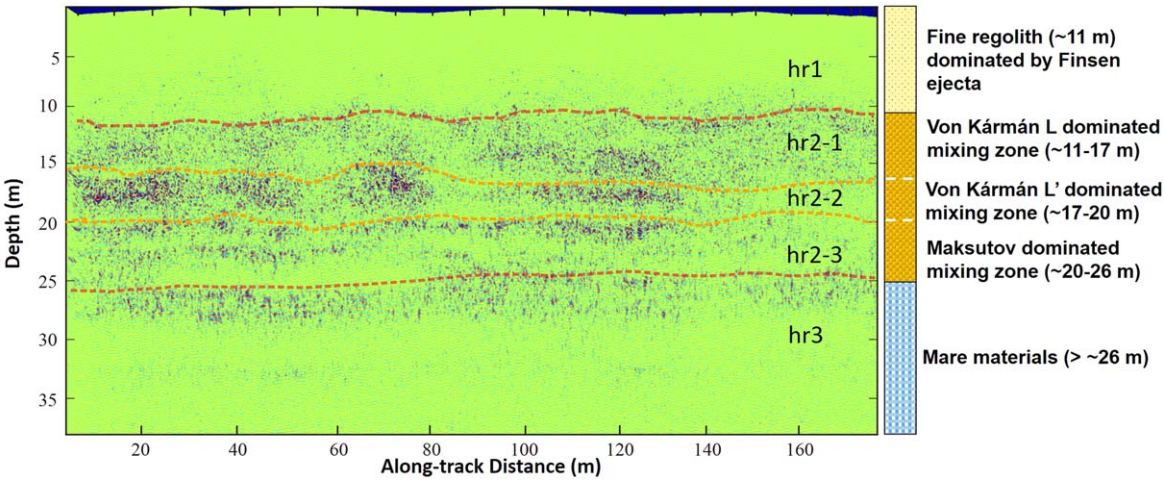


Figure 7. The first five lunar days of the LPR radargram of Yutu-2 and the resultant geologic interpretations. The LPR data were processed with repetitive data removal, including filtering, background removal, amplitude compensation, migration, and topographic correction. The topographic correction is referenced to the elevation of the landing site. For further details, refer to Lai et al. (2019, 2020). "hr" stands for horizontal reflector, hr1 for fine-grained regolith dominated by Finsen ejecta, hr2-1 for a mixture zone dominated by Von Kármán L ejecta, hr2-2 for a mixture zone dominated by Von Kármán L′ ejecta, hr2-3 for a mixture zone dominated by Maksutov ejecta, and hr3 for local mare basalts. All the hr1, hr2-1, hr2-2, and hr2-3 layers also contain Finsen ejecta, pre-existing ejecta, and local mare materials.

SPA ejecta deposits and excavate a large mass of crustal materials. This result indicates that the ejecta of many large craters in the SPA region may be a mixture of mafic-rich and mafic-poor materials.

5.3. Comparison between the Model-derived Stratigraphy and the LPR Observations

The first five lunar days of the LPR observations of Yutu-2 show three distinct subsurface layers ∼40 m deep, possibly corresponding to a fine-grained regolith layer, a layer of ejecta deposits, and a layer of possible mare basalts (hr1, hr2, and hr3 in Figure 7; Lai et al. 2019). On the basis of the CE-4 in situ radar measurements, only the stratigraphy estimated from Pike's model (22.1 m in total thickness) are consistent with the LPR observations (Figure 7), while the ejecta deposit thicknesses estimated from the other three models (6.4 m for McGetchin's model, 14.0 m for Housen's model, and 10.7 m for Sharpton's model) are far thinner than the sum thickness of hr1 and hr2 of the LPR observations. This is also consistent with several previous studies (e.g., Krüger et al. 2014; Xie & Zhu 2016; Xu & Xie 2020) that showed that Pike's model gives better constraints on the distribution of primary ejecta than other models. In particular, since the impact ejecta deposits on mare basalts at the CE-4 landing site are no thicker than 30 m, we confirmed that the hr3 layer (∼26–40 m deep) should not be ejecta deposits but mare basalts.

Therefore, our estimates based on Pike's model show that the hr1, hr2, and hr3 layers reflected in radar measurements can correspond to a fine-grained regolith layer (0–∼11 m deep) dominated by Finsen ejecta, a combination layer (∼11–26 m deep) of coarse ejecta deposits (i.e., the mixture zone of Finsen's primary ejecta, pre-Finsen primary ejecta, and local basalt materials), and a local mare basalt layer (∼26–40 m deep; Figure 7), respectively. Since the true mixture scenario should be located between the no mixing (Figure 5(a)) and homogenous mixing scenarios (Figure 6(a)), the Finsen ejecta would not completely mix with ejecta from previous craters and the layers dominated by previous ejecta may still exist. The second layer (hr2 in Figure 7) observed in the first five lunar days of the LPR observations can be further divided into three sublayers of ∼11–17 m, ∼17–20 m, and ∼20–26 m deep (hr2-1, hr2-2, and hr2-3 in Figure 7(c)), which also correspond well to the mixing zones dominated by Von Kármán L ejecta, Von Kármán L′ ejecta, and Maksutov ejecta, respectively. Each sublayer is mixed with Finsen ejecta and prematerials (Figure 7).

6. Conclusions

In this study, we examined all possible sources (post-mare craters) of foreign materials on the mare basalts at the CE-4 landing site and found 16 craters potentially delivering primary ejecta >10 cm level in thickness based on Pike's model. The total ejecta thicknesses of these 16 craters are 18.6 m, 5.7 m, 12.7 m, and 9.0 m based on the models of Pike (1974), McGetchin et al. (1973), Housen et al. (1983), and Sharpton (2014), respectively.

Four craters are principal foreign material sources to the CE-4 landing site based on Pike's model: Finsen (9.4 m thick), Von Kármán L (3.2 m thick), Von Kármán L′ (2.1 m thick), and Maksutov (1.1 m thick). Their most likely emplacement sequence is: Maksutov, Von Kármán L′, Von Kármán L, and Finsen from older to younger. Finsen ejecta should be the most dominant materials from the surface to several meters deep at the CE-4 landing site with a ratio of at least 43% regardless of the model choice, as long as the regolith layer is thinner than the ejecta deposits of Finsen, which is consistent with the VNIS observations of Yutu-2 (Huang et al. 2018; Hu et al. 2019).

Taking the local material excavations and mixtures into consideration, these four principal source craters produce ejecta deposits at the CE-4 landing site with total thicknesses of 22.1 m, 6.4 m, 14.0 m, and 10.7 m based on the ejecta models of Pike (1974), McGetchin et al. (1973), Housen et al. (1983), and Sharpton (2014), respectively. All the post-mare impact ejecta upon local mare basalts at the CE-4 landing site is estimated to be thinner than 30 m.

The ejecta thicknesses estimated from Pike's model are the most consistent with the first five lunar days of the Yutu-2 LPR observations compared with the other three models and the five

layers reflected in the LPR observations (from 0 to ∼40 m deep) correspond well to a fine regolith layer, a Von Kármán L-dominant mixing zone, a Von Kármán L′-dominant mixing zone, a Maksutov-dominant mixing zone, and a local mare basalt layer.

The authors thank Dr. Minggang Xie for valuable discussions when writing the manuscript. This work was supported by the pre-research project on Civil Aerospace Technologies No. D020202 funded by China National Space Administration (CNSA), the Science and Technology Development Fund of Macau (0079/2018/A2), the National Key R&D Program of China (No. 2020YFE0202100), the pre-research project on Civil Aerospace Technologies No. D020204 funded by CNSA, the Science and technology project of Jiangxi education department (Grant GJJ200821), and the Scientific Research Starting Foundation for scholars from Jiangxi University of Science and Technology (Grant jxxjbs18017). All LROC and LOLA data can be downloaded from the USGS Astrogeology Science Center (https://astrogeology.usgs.gov/maps/) and CE-2 Digital Orthophoto Map (DOM) 7 m data are available at the Data Release and Information Service System of China's Lunar Exploration Program (http://moon.bao.ac.cn).

ORCID iDs

Luyuan Xu https://orcid.org/0000-0003-4708-7441
Xunyu Zhang https://orcid.org/0000-0002-5197-9410
Le Qiao https://orcid.org/0000-0002-6180-2344
Jialong Lai https://orcid.org/0000-0002-2157-2767

References

Baldwin, R. B. 1963, The Measure of the Moon (Chicago, IL: Univ. Chicago Press)
Bandfield, J. L., Ghent, R. R., Vasavada, A. R., et al. 2011, JGRE, 116, E12
Bart, G. D., Nickerson, R. D., Lawder, M. T., et al. 2011, Icar, 215, 485
Croft, S. K. 1985, JGR, 90, C828
Fa, W., Liu, T., Zhu, M. H., et al. 2014, JGRE, 119, 1914
Fortezzo, C. M., Spudis, P. D., & Harrel, S. L. 2020, LPI, 2326, 2760
Garrick-Bethell, I., & Zuber, M. T. 2009, Icar, 204, 399
Ghent, R. R., Hayne, P. O., Bandfield, J. L., et al. 2014, Geo, 42, 1059
Haruyama, J., Ohtake, M., Matsunaga, T., et al. 2009, Sci, 323, 905
Haskin, L. A., Moss, B. E., & McKinnon, W. B. 2003, M&PS, 38, 13
Housen, K. R., Schmidt, R. M., & Holsapple, K. A. 1983, JGRB, 88, 2485
Hu, X., Ma, P., Yang, Y., et al. 2019, GeoRL, 46, 9439
Huang, J., Xiao, Z., Flahaut, J., et al. 2018, JGRE, 123, 1684
Krüger, T., Sturm, S., & Kenkmann, T. 2014, Proc. LPSC, 45, 1834
Lai, J., Xu, Y., Bugiolacchi, R., et al. 2020, NatCo, 11, 1
Lai, J., Xu, Y., Zhang, X., et al. 2019, GeoRL, 46, 12783
Li, C., Liu, D., Liu, B., et al. 2019, Natur, 569, 378
Li, C., Su, Y., Pettinelli, E., et al. 2020, SciA, 6, eaay6898
Ling, Z., Qiao, L., Liu, C., et al. 2019, P&SS, 179, 104741
Losiak, A., Wilhelms, D. E., Byrne, C. J., et al. 2009, LPI, 40, 1532
McGetchin, T. R., Settle, M., & Head, J. W. 1973, E&PSL, 20, 226
Melosh, H. J. 1989, Impact Cratering: A Geologic Process (Oxford: Oxford Univ. Press), 245
Oberbeck, V. R., Hörz, F., Morrison, R. H., et al. 1975, Moon, 12, 19
Pasckert, J. H., Hiesinger, H., & van der Bogert, C. H. 2018, Icar, 299, 538
Petro, N. E., & Pieters, C. M. 2004, JGRE, 109, E6
Petro, N. E., & Pieters, C. M. 2006, JGRE, 111, E9
Petro, N. E., & Pieters, C. M. 2008, M&PS, 43, 1517
Pike, R. J. 1974, E&PSL, 23, 265
Pike, R. J. 1980, Proc. LPSC, 11, 2159
Quaide, W. L., & Oberbeck, V. R. 1968, JGR, 73, 5247
Robbins, S. J. 2019, JGRE, 124, 871
Sharpton, V. L. 2014, JGRE, 119, 154
Spudis, P. D., Gillis, J. J., & Reisse, R. A. 1994, Sci, 266, 1848
Stöffler, D., & Ryder, G. 2001, Chronology and Evolution of Mars (Dordrecht: Springer), 9
Stuart-Alexander, D. E. 1978, US Geological Survey, Map I-1047
Wilhelms, D. E., & Byrne, C. J. 2009, Index of Strata, http://www.imageagain.com/Strata/
Xie, M., Liu, T., & Xu, A. 2020a, JGRE, 125, e06113
Xie, M., Xiao, Z., Zhang, X., et al. 2020b, JGRE, 125, e06112
Xie, M., & Zhu, M.-H. 2016, E&PSL, 440, 71
Xu, L., & Xie, M. 2020, JGRE, 125, e06506
Yingst, R. A., Chuang, F. C., Berman, D. C., et al. 2017, LPI, 1964, 1680
Yingst, R. A., & Head, J. W., III 1997, JGRE, 102, 10909
Zhang, J., Zhou, B., Lin, Y., et al. 2021a, NatAs, 5, 25
Zhang, X., Xie, M., & Xiao, Z. 2021b, Icar, 358, 114214